Effects of Gravity Wave Drag Induced by Cumulus Convection on the Atmospheric General Circulation

HYE-YEONG CHUN, MYUNG-DUK SONG, AND JEONG-WOO KIM

Department of Atmospheric Sciences and Global Environment Laboratory, Yonsei University, Seoul, Korea

JONG-JIN BAIK

Department of Environmental Science and Engineering, Kwangju Institute of Science and Technology, Kwangju, Korea

(Manuscript received 6 December 1999, in final form 15 May 2000)

ABSTRACT

A parameterization scheme of gravity wave drag induced by cumulus convection (GWDC) is implemented in the Yonsei University atmospheric general circulation model (GCM) and the effects of GWDC on the zonal-mean flow and planetary waves are investigated through perpetual July simulations. The GWDC parameterization scheme used in this study includes a momentum gain in the cloud region to conserve the momentum.

The gravity wave stress at the cloud top is concentrated in the intertropical convergence zone (ITCZ) with its maximum value of 0.14 N m^{-2} near the tropopause due to deep cumulus clouds. The wave breaking occurs mainly in the upper troposphere and lower stratosphere. The maximum westerly acceleration in the ITCZ is 0.6 m s^{-1} day^{-1}, which is close to that observed. It is surprising to observe that the zonal wind difference between the simulations with and without the GWDC parameterization is largest in the Southern Hemisphere (SH) midlatitude stratosphere, where a westerly jet exists, rather than in the major drag forcing region and that there is an associated warming in the SH polar stratosphere. The excessive westerly jet in the SH that appears in the simulation without the GWDC parameterization is alleviated significantly (7 m s^{-1}) by its inclusion. This result implies that the nonlinear process through planetary waves rather than by direct drag forcing might play an important role in changing the zonal-mean flow. The analysis of the geopotential height perturbation reveals that the amplification of the waves of zonal wavenumbers 1 and 2 in the SH stratosphere is responsible for the change in the zonal-mean flow there. In particular, the wave amplitude of zonal wavenumber 2 significantly increases (more than three times) by the GWDC process in the SH midlatitude upper stratosphere.

It is suggested that understanding interactions between the gravity wave drag, zonal-mean flow, and planetary waves is necessary to better parameterize the gravity wave drag. This study is particularly encouraging in that including the GWDC parameterization can alleviate the excessive westerly bias in the SH midlatitude and its associated cold temperature bias in the SH polar region reported for many GCMs.

1. Introduction

The effects of gravity wave drag (GWD) on atmospheric general circulation have received much attention during the last decade. It has become recognized that GWD is an important subgrid-scale dynamic process that should be included in general circulation models (GCMs) for the observed large-scale flows to be better simulated. The systematic model errors such as the westerly bias in the Northern Hemisphere (NH) wintertime mean flow and its associated cold temperature bias in the polar region could be successfully alleviated by including an orographically induced GWD parameterization (Palmer et al. 1986; McFarlane 1987). However, in the Southern Hemisphere (SH) where mountain-drag effects are relatively small, the systematic model biases of excessive westerly jet in the upper stratosphere and cold temperature in the polar region still remain (Manzini and Bengtsson 1996).

Even though GWD parameterization employed in most GCMs is based on mountain-induced internal gravity waves, considerable uncertainties of the sources of gravity waves in the troposphere still exist. Fritts (1984) pointed out that a large portion of observed gravity waves in the upper atmosphere has higher frequencies than stationary mountain waves. Cumulus convection can be a possible source of high-frequency waves. Cumulus clouds impinging on a stably stratified stratosphere generate internal gravity waves that influence the

Corresponding author address: Prof. Hye-Yeong Chun, Department of Atmospheric Sciences, Yonsei University, Shinchon-dong, Seodaemun-ku, Seoul 120-749, Korea.
E-mail: chy@atmos.yonsei.ac.kr

large-scale flow through gravity wave drag. The effects of vertically propagating internal gravity waves induced by convection might be dominant in the tropical region where persistent cumulus clouds exist. Recently, convectively generated internal gravity waves and their effects on the large-scale flow have been studied using observational data (Pfister et al. 1993) and cloud-resolving models (Fovell et al. 1992; Alexander and Holton 1997) in conjunction with a possible mechanism for quasi-biennial oscillation (QBO). Also, ways to parameterize GWD by convection in large-scale models have been proposed (Kershaw 1995; Chun and Baik 1998, CB hereafter).

Two GWD parameterization methods are in use for numerical models. The first method deals with the sources of gravity waves explicitly and parameterizes GWD based on the momentum flux of gravity waves induced by a specific wave source. Mountain-induced GWD parameterization schemes (e.g., Palmer et al. 1986) usually adopt this methodology. Rind et al. (1988a) parameterized GWD by specifying momentum fluxes due to mountain, shear instability, and moist convection based on the formulation of Lindzen (1984). Recently, Kershaw (1995) and CB proposed ways to parameterize GWD induced by convective clouds in large-scale models based on this methodology. Using a linear, monochromatic internal gravity wave theory, Kershaw (1995) formulated the momentum flux by convectively generated internal gravity waves under the assumption that the wave energy above the convective region is proportional to the convective kinetic energy in the cloud region. Chun and Baik (1998) derived an analytical formulation of the momentum flux by internal gravity waves induced by specified diabatic forcing, which represents the latent heating of cumulus convection, and proposed a parameterization scheme using the wave saturation hypothesis of Lindzen (1981). Their formulation of the momentum flux at the cloud top is surprisingly analogous to that of GWD generated by mountains when the Froude number in the mountain drag formulation is replaced by the nonlinearity factor of thermally induced internal gravity waves.

The second method is called gravity wave spectrum method based on a linear, monochromatic wave theory. In this method, a deposition of the momentum transported by gravity waves is considered to result from the breaking of individual wave mode interacting with the mean flow. Holton (1983) was the first to attempt to parameterize GWD based on the wave saturation hypothesis of Lindzen (1981). Recently, a similar parameterization scheme was implemented in GCMs by Hamilton (1997) and Norton and Thuburn (1997). This parameterization scheme was improved by including nonlinearity between waves (Hines 1991) and anisotropy in the wave spectrum (Medvedev and Klaassen 1995; Medvedev et al. 1998). Even though this scheme can take into account a wide distribution of wave spectra, source mechanisms cannot be explicitly considered. That is, the spatial and temporal distribution of gravity waves that appears in the real atmosphere by various tropospheric sources cannot be accounted for in principle. This limitation might be relaxed to some extent by producing realistic gravity wave spectrum constructed using observational data (Allen and Vincent 1995) or cloud-resolving model data (Alexander et al. 1995; Alexander and Holton 1997).

In this study, the GWD parameterization scheme proposed by CB is implemented in the YONU GCM (Yonsei University Atmospheric General Circulation Model) to examine the effects of GWD induced by cumulus convection (GWDC hereafter) on the zonally averaged flow and planetary waves through perpetual July simulations. In section 2, an implementation procedure of the GWDC parameterization of CB, which is slightly modified, is given. A description of the YONU GCM and experimental design are given in section 3. Simulation results are presented and discussed in section 4. Summary and conclusions are given in section 5.

2. Convection-induced gravity wave drag parameterization

For a GWDC parameterization, we adopted a scheme proposed by CB with a slight modification. Chun and Baik (1998) obtained an analytical formulation of the momentum flux profile based on the two-dimensional, linear, steady-state response of a stably stratified flow to specified thermal forcing. In their formulation, the momentum flux is zero from the surface to the cloud base because of the cancellation of upward and downward propagating waves, varies with height in the cloud region, and remains constant above the cloud top. Gravity waves can change the large-scale flow through the vertical convergence/divergence of the momentum flux in the cloud region and through the wave breaking process above the cloud top. However, when GWDC is parameterized in GCMs, the momentum flux in the cloud region is not considered because subgrid-scale cumulus convection represented as a thermal forcing in the analytical formulation is activated only in the conditionally unstable atmosphere in GCMs. In reality, the momentum flux in the cloud region is generated mainly by clouds with turbulent characteristics rather than by internal gravity waves. The effects of the cloud momentum flux in the cloud region on the large-scale flow are better included in cumulus parameterization schemes as suggested by Wu and Moncrieff (1996) and Gregory et al. (1997).

However, a compensating deceleration or acceleration of the large-scale flow in the cloud region should be taken into account in order to close the momentum budget. There exists a fundamental difference between wave drag induced by cumulus convection and that by mountains in how to close the momentum budget. In the case of mountain wave drag, the momentum removed aloft is lost by the atmosphere as it is transferred to the solid

earth. Unlike mountain wave drag, in the case of wave drag induced by cumulus convection, the momentum transfer occurs within the atmosphere. That is, any momentum removed aloft should be compensated by a gain in the cloud region. Kershaw (1995) raised this problem and showed that the gravity wave momentum flux transferred downward is deposited to the upper part (within 2 km) of clouds. However, CB did not explicitly mention the problem in closing the momentum budget in their parameterization. The only justification for neglecting this effect is that the larger density in lower layer makes its acceleration insignificant. In the present study, the GWDC parameterization scheme of CB is improved by including a momentum deposition in the cloud region.

The effects of subgrid-scale gravity wave drag can be included in the horizontal momentum equations by

$$\frac{\partial u}{\partial t} = -\frac{1}{\rho}\frac{\partial \tau_x}{\partial z}, \tag{1}$$

$$\frac{\partial \upsilon}{\partial t} = -\frac{1}{\rho}\frac{\partial \tau_y}{\partial z}, \tag{2}$$

where u and υ are the zonal and meridional components of wind, respectively; ρ is the air density; and τ_x and τ_y are the zonal and meridional components of the subgrid-scale momentum flux, respectively. A procedure for calculating τ_x and τ_y at each model level can be summarized in connection with the Arakawa–Schubert cumulus parameterization (Arakawa and Schubert 1974) as follows:

1) Calculate the wave stress vector at the cloud-top level ($\boldsymbol{\tau}_{ct}$) for each individual cloud in a grid box as

$$\boldsymbol{\tau}_{ct} = -\frac{\rho_{ct}|\mathbf{u}_{ct}|^2}{N\Delta x}\mathbf{u}_{ct}c_1c_2^2\mu_{ct}^2, \tag{3}$$

$$\mu_{ct} = \frac{gQ_0a_1}{c_pNT|\mathbf{u}_{ct}|^2}, \tag{4}$$

where Q_0/c_p is the diabatic heating rate (K s^{-1}) by subgrid-scale cumulus cloud (Q_0 is the amplitude of diabatic forcing and c_p is the specific heat at constant pressure), N the buoyancy frequency, T the temperature, $\mathbf{u}_{ct}$ the horizontal wind vector at the cloud top, ρ_{ct} the air density at the cloud top, Δx the horizontal grid size, g the gravitational acceleration, a_1 the approximate horizontal scale of effective cloud, and c_1 and c_2 are constants related to the horizontal and vertical structures of the diabatic forcing, respectively. All the variables except for Q_0 in (3) and (4) are evaluated at the cloud-top level. Even though Q_0 in (4) is assumed to be constant with height in CB, the maximum value of Q in the vertical profile of convective heating rate produced by the GCM in each grid box is used for Q_0. Following CB, $c_1 = 1.41$ and $c_2 = -0.28$ are used. Here a_1 is approximated by $\alpha\Delta x$, where α is the fractional coverage of cloud within a grid box. In simulations, $\alpha = 0.4$ is assumed for the total subensemble clouds within a grid box. Since (3) and (4) are applied for each subensemble cloud, $a_1 = \alpha\Delta x/n$, where n is the total number of subensemble clouds within a grid box, is used.

2) The stress τ at any level parallel to the stress vector at the cloud-top level can be written as

$$\tau = \left[\frac{\rho U^3}{N\Delta x}\right]c_1c_2^2\mu^2, \tag{5}$$

$$\mu = \frac{gQ_0a_1}{c_pNTU^2}, \tag{6}$$

where U is the magnitude of the component of the wind vector $\mathbf{u}$ in the direction of the stress at the cloud top [$U = (\mathbf{u}\cdot\boldsymbol{\tau}_{ct})/|\boldsymbol{\tau}_{ct}|$].

3) Define the minimum Richardson number including wave effect as

$$\mathrm{Ri}_{\min} = \frac{\mathrm{Ri}(1 - \mu|c_2|)}{(1 + \mu\mathrm{Ri}^{1/2}|c_2|)^2}, \tag{7}$$

where Ri is the local Richardson number.

4) Check whether wave breaking occurs based on the minimum Richardson number given by (7). That is, if $\mathrm{Ri}_{\min} \geq \frac{1}{4}$, then τ at the level above cloud is set to τ_{ct}. If $\mathrm{Ri}_{\min} < \frac{1}{4}$, then $\mathrm{Ri}_{\min}$ is set to $\frac{1}{4}$ using the wave saturation hypothesis of Lindzen (1981) and the saturation stress is calculated using

$$\tau_s = \left[\frac{\rho U^3}{N\Delta x}\right]c_1c_2^2\mu_s^2, \tag{8}$$

$$\mu_s = \frac{1}{|c_2|}\left[2\sqrt{2 + \frac{1}{\sqrt{\mathrm{Ri}}}} - \left(2 + \frac{1}{\sqrt{\mathrm{Ri}}}\right)\right]. \tag{9}$$

5) Repeat the previous steps 2, 3, and 4 at the next higher level unless either τ approaches zero or the model top reaches.

6) Determine the stress components in the x and y directions by

$$\tau_x = \tau\cos\theta, \qquad \tau_y = \tau\sin\theta, \tag{10}$$

where θ is the angle between the cloud-top stress vector and the zonal direction.

7) Calculate a deposition of the momentum in a cloud region for the momentum conservation by computing vertically integrated momentum above the subensemble cloud. Following Kershaw (1995), it is assumed that the momentum is deposited only within the layer between the cloud-top level and the level just below the cloud-top level. Then, the acceleration in the cloud region is obtained from the momentum conservation:

$$\int_{\sigma_{ct+1}}^{\sigma_{ct}} \rho\left(\frac{\partial u}{\partial t}\right) d\sigma = -\int_{\sigma_{ct}}^{\sigma_1} \rho\left(\frac{\partial u}{\partial t}\right) d\sigma, \tag{11}$$

$$\int_{\sigma_{ct+1}}^{\sigma_{ct}} \rho\left(\frac{\partial \upsilon}{\partial t}\right) d\sigma = -\int_{\sigma_{ct}}^{\sigma_1} \rho\left(\frac{\partial \upsilon}{\partial t}\right) d\sigma, \tag{12}$$

where σ_1, σ_{ct}, and σ_{ct+1} represent the model top, the

cloud top, and the level just below the cloud top, respectively.

8) Take a summation over all subensemble clouds to obtain

$$\frac{\partial u}{\partial t} = \sum_{i=1}^{n} \left(\frac{\partial u}{\partial t}\right)_i, \tag{13}$$

$$\frac{\partial v}{\partial t} = \sum_{i=1}^{n} \left(\frac{\partial v}{\partial t}\right)_i, \tag{14}$$

where n is again the total number of subensemble clouds in a grid box and $(\partial u/\partial t)_i$ and $(\partial v/\partial t)_i$ are the zonal and meridional accelerations by the ith subensemble cumulus cloud, respectively. The GWDC parameterization can be easily implemented in models that include cumulus parameterization schemes other than the Arakawa–Schubert-type scheme, if one follows the essence of the procedure described above.

3. Model description and experimental design

The GWDC parameterization scheme described in section 2 is implemented in the YONU GCM. The model has 15 layers in the vertical with 8 layers of the troposphere and 7 layers of the stratosphere and has horizontal grid spacing of 4° lat × 5° long. The vertical coordinate is a modified σ coordinate with the model top at 1 mb. The atmospheric prognostic variables are surface pressure, zonal and meridional winds, temperature, water vapor mixing ratio, and cloud water mixing ratio. Other prognostic variables are ground temperature, ground moisture over land surface, and accumulated snow mass over land and ice surfaces. For spatial differencing, the Arakawa C-grid system is employed for the horizontal differencing and the C′-grid system (Tokioka 1978) for the vertical differencing. For time differencing, the leapfrog scheme is used with the Matsuno scheme inserted at regular intervals.

The short- and longwave radiation parameterization schemes are based on Oh (1989), which include a two-stream delta-Eddington approximation to deal with absorption and scattering by clouds and gases. Three types of clouds are parameterized: stratiform cloud, convective cloud, and planetary boundary layer (PBL) cloud. The parameterization of stratiform cloud basically follows Sundqvist (1988) and the PBL cloud is parameterized quasi-prognostically based on the cloud-topped mixed layer model of Lilly (1968) and Guinn (1989). The convective cloud parameterization is based on the Arakawa–Schubert scheme (Arakawa and Schubert 1974) modified by Oh (1989). For the midlevel convection, the moist convective adjustment is carried out. The PBL is parameterized following Randall (1976). Surface fluxes of sensible and latent heat are calculated using the bulk aerodynamic method by Louis (1979) and the single-layer bucket model (Manabe 1969) is used for land surface hydrology. Gravity wave drag induced by mountains is parameterized following Palmer et al. (1986). The horizontal diffusion of momentum is computed following Holloway and Manabe (1971) and the vertical diffusion of momentum, sensible heat, and water vapor is treated following Oh (1989). Table 1 gives a brief description of the YONU GCM.

TABLE 1. A brief description of the YONU GCM.

Feature	Description
Horizontal differencing	Finite difference 4° lat × 5° long Arakawa C-grid system
Vertical differencing	σ-coordinate 15-layer (8-layer troposphere + 7-layer stratosphere) Model top of 1 mb C′-grid system (Tokioka 1978)
Time differencing	Leapfrog scheme + Matsuno scheme (1st step of each hour) Δt = 7.5 min.
Diffusion	Horizontal diffusion (Holloway and Manabe 1971) Vertical diffusion (Oh 1989)
Shortwave radiation	Two-stream/delta-Eddington approximation (Oh 1989)
Longwave radiation	Two-stream approximation (Oh 1989)
Deep convection	Modified Arakawa-Schubert scheme (Oh 1989)
Large-scale condensation	Sundqvist (1988)
Large-scale evaporation	Schlesinger et al. (1988)
PBL cloud	Lilly (1968), Guinn (1989)
Planetary boundary layer	Randall (1976)
Surface fluxes	Bulk aerodynamic method (Louis 1979)
Land surface hydrology	Single-layer bucket model (Manabe 1969)
Gravity wave drag	Gravity wave drag by mountains (Palmer et al. 1986; Chun et al. 1996) Gravity wave drag by convection (Chun and Baik 1998)

Numerical simulations are performed for perpetual July. The model is integrated for 360 days using the initial fields at 0000 UTC 1 July 1986. Results presented below are the last 90-day-averaged fields. For the perpetual simulations, the seasonal variation of solar insolation is excluded and the climatological monthly mean sea surface temperature (Alexander and Mobley 1976) is used. For the ozone distribution, zonally averaged monthly mean climatological data are used. In order to investigate the effects of GWDC on the atmospheric general circulation in the GCM, two simulations are performed: control simulation without the GWDC parameterization and GWDC simulation with the GWDC parameterization. Note that the mountain-induced gravity wave drag parameterization of Palmer et al. (1986) is included in both the simulations. The observed data used for comparison with simulation results are the National Centers for Environmental Prediction (NCEP) reanalysis data of 19-yr (1979–97) monthly means for July. However, since the NCEP re-

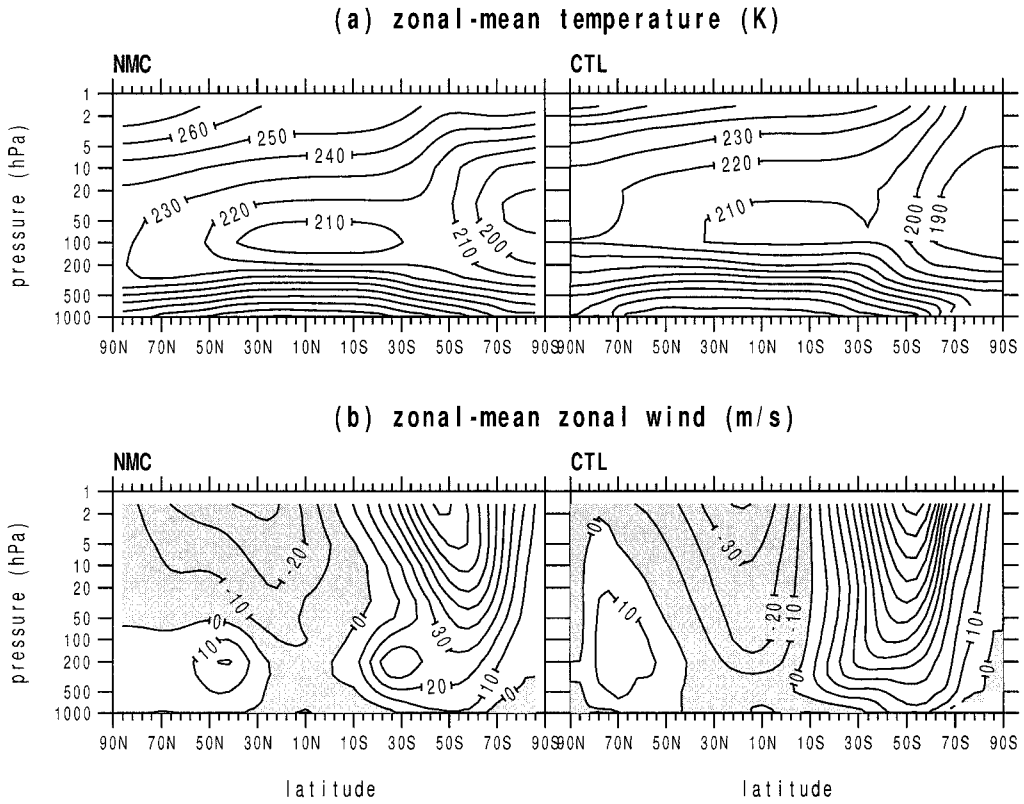

FIG. 1. The latitude–height cross section of the (a) zonal-mean temperature and (b) zonal-mean zonal wind for the 14-yr averaged July in the NMC analysis (left panels) and the last 90-day averaged perpetual July in the control simulation (right panels). The contour intervals in (a) and (b) are 10 K and 10 m s^{-1}, respectively. The negative values in (b) are shaded.

analysis data cover only up to 10 mb, another 14-yr (1979–92) July means up to 1 mb produced by the National Meteorological Center (NMC, now known as NCEP) are used for the comparison in zonal-mean temperature and wind fields.

4. Results and discussion

a. Control simulation

Figure 1 shows the zonal-mean temperature and zonal wind fields of the 14-yr-averaged NMC analysis and control simulation. In the troposphere, the observed zonal-mean temperature decreases rapidly with height and decreases latitudinally from the equator to high latitude with a cold region near the equatorial tropopause. In the stratosphere, the zonal-mean temperature is minimum in the lower stratospheric polar region of the winter hemisphere and is maximum in the upper-stratospheric polar region of summer hemisphere. The simulated zonal-mean temperature is in good agreement with observations except that near the polar regions of both hemispheres the simulated temperature is lower than the observed by about 10 K. The cold bias in the high-latitude stratosphere is a common feature in many climate models (e.g., Manzini and Bengtsson 1996; Stratton 1999). Recently, Stratton (1999) showed that increasing model resolution did not fundamentally remove the cold bias. It is well known that including mountain-induced GWD parameterization can significantly alleviate the cold bias in the NH wintertime polar region (Palmer et al. 1986). However, the effects of mountain-induced GWD are relatively small in the NH summertime compared to those in the NH wintertime due to the weak stability and wind near the surface. The effects are also small in the SH.

The corresponding zonal-mean zonal wind field is shown in Fig. 1b. The simulated SH stratospheric jet is too strong and the subtropical jet in the SH is not apparent due to poor separation. In the NH, the westerly region extends too high and the intensity of easterlies in the upper stratosphere is stronger than the observed by about 10 m s^{-1}. This discrepancy in the zonal-mean zonal wind is closely connected with the zonal-mean temperature through the thermal wind relationship. It is common for GCMs to produce strong westerly jet bias in the SH wintertime, even though westerly jet in the NH wintertime is relatively well simulated when mountain-induced GWD parameterization is included. To improve the zonal wind field in the SH wintertime, a cer-

tain physically based drag process similar to mountain-induced GWD in the NH appears to be necessary. This is one of the reasons for taking into account convectively generated gravity wave drag in the present study. In this study, we will not carry out the detailed performance analyses of the YONU GCM. Rather, we will emphasize the effects of GWDC on the simulated zonal-mean flow and planetary waves by comparing the results of the control and GWDC simulations.

b. GWDC simulation

1) GRAVITY WAVE STRESS AT CLOUD TOP

The influence of GWDC on the large-scale flow can be represented by the gravity wave stress at the cloud top because the maximum change in the mean wind through the wave breaking directly depends on its magnitude. Although the mountain drag is measured in several field experiments (e.g., Hoinka 1985), there is not enough observational evidence for the cloud-top wave stress. Pfister et al. (1993) tried to measure the gravity wave momentum flux excited by convection. Unfortunately, it is not easy to directly compare their observed momentum flux with the cloud-top wave stress introduced in this study. However, they showed that the maximum westerly acceleration by convectively generated gravity waves in the stratosphere is about 0.4 m s^{-1} day^{-1}. An alternative way to overcome the lack of observational data for convectively generated gravity waves above clouds is to use simulation data obtained using cloud-resolving models. The numerical modeling studies of convectively generated internal gravity waves (e.g., Fovell et al. 1992; Kershaw 1995) revealed that the magnitude of the cloud-top wave stress is on the order of 0.1–0.2 N m^{-2}. Although this magnitude is smaller than an averaged mountain drag of about 1 N m^{-2}, the large-scale flow in the stratosphere can be changed significantly. Another alternative way to estimate the magnitude of gravity wave drag forcing is based on the zonal-mean momentum budget using observational data (e.g., Hamilton 1983; Smith and Lyjak 1985). However, most of the studies are for the NH wintertime situation [four Januaries in Hamilton (1983) and October–May in Smith and Lyjak (1985)].

Figure 2 shows the global distribution of the cloud-top gravity wave stress vector and its magnitude at levels 9–13 calculated using (3) and (4). It was found that there are a few grid points where the instantaneous magnitude of the cloud-top wave stress is larger than 20 N m^{-2} during the numerical integration mainly due to the weak static stability and/or horizontal wind. To avoid numerical instability in such a situation, its magnitude is constrained not to exceed 20 N m^{-2}. Note that the magnitude of the cloud-top wave stress is inversely proportional to N^3 and $|\mathbf{u}_{ct}|$. This is one of the main differences between mountain drag, in which the magnitude is proportional to the horizontal wind speed and stability, and GWDC. Since the GWDC parameterization scheme used in this study is applied to individual subensemble cumulus cloud with different cloud-top height in a GCM gird box, the cloud-top wave stress can be obtained approximately from the top of the PBL (~level 13) to the tropopause (~level 8). However, since the magnitude of the cloud-top wave stress is very small ($\sim 10^{-5}$ N m^{-2}) at level 8 compared to other levels 9–13, the cloud-top wave stress is shown up to level 9 in Fig. 2. As expected, the cloud-top wave stress is large with a maximum value of -0.14 N m^{-2} at level 9 in the intertropical convergence zone (ITCZ) from 10°S to 30°N where persistent deep cumulus clouds exist. The cloud-top wave stress by midlevel cumulus clouds (levels 10 and 11) is distributed over a large portion of NH land areas as well as the ITCZ. In the SH midlatitude, the cloud-top wave stress is mainly due to midlevel and shallow cumulus clouds, but its magnitude is very small compared to that by deep cumulus clouds.

Because a realistic global production of the cloud-top gravity wave stress is crucial in the GWDC parameterization, the simulation result in Fig. 2 is roughly compared to observation. Figure 3 shows the global distribution of the maximum convective heating rate and the cloud-top gravity wave stress. The cloud-top wave stress is calculated using (3) and (4) using the observed wind and temperature fields at 200 mb and the maximum convective heating rate (Fig. 3a) from the NCEP reanalysis data. Major convective heating regions are observed in the ITCZ and relatively weak convective heating regions exist in the NH middle and high latitudes. The regions of strong wave stress at 200 mb are coincident with the major convective regions. Since strong stability and horizontal wind in high latitude significantly reduce the magnitude of the wave stress, the wave stress is concentrated in the ITCZ. The model produces convection in northern Africa rather than in central Africa and the maximum magnitude of the wave stress at 200 mb is about a half of that in the observation (0.25 N m^{-2}). However, the simulated regions of deep cumulus clouds and wave stress at 200 mb are in reasonable agreement with the observation.

2) ZONAL-MEAN DIFFERENCE BY GWDC

Figure 4 shows the zonal-mean zonal wind tendency field due to the GWDC parameterization. There exists a region of westerly acceleration in the upper troposphere between 10°S and 30°N where deep cumulus clouds exist as shown in Figs. 2 and 3. The maximum acceleration in that region is 0.6 m s^{-1} day^{-1}. This value is close to that observed by Pfister et al. (1993) (0.4 m s^{-1} day^{-1}), but is much smaller than that obtained using a cloud-resolving model by Alexander et al. (1995) (5 m s^{-1} day^{-1}). This is expected because the convective heating rate in the GCM with cumulus parameterization is smaller than that in the cloud-resolving model with explicit cloud microphysical processes. Since the zonal

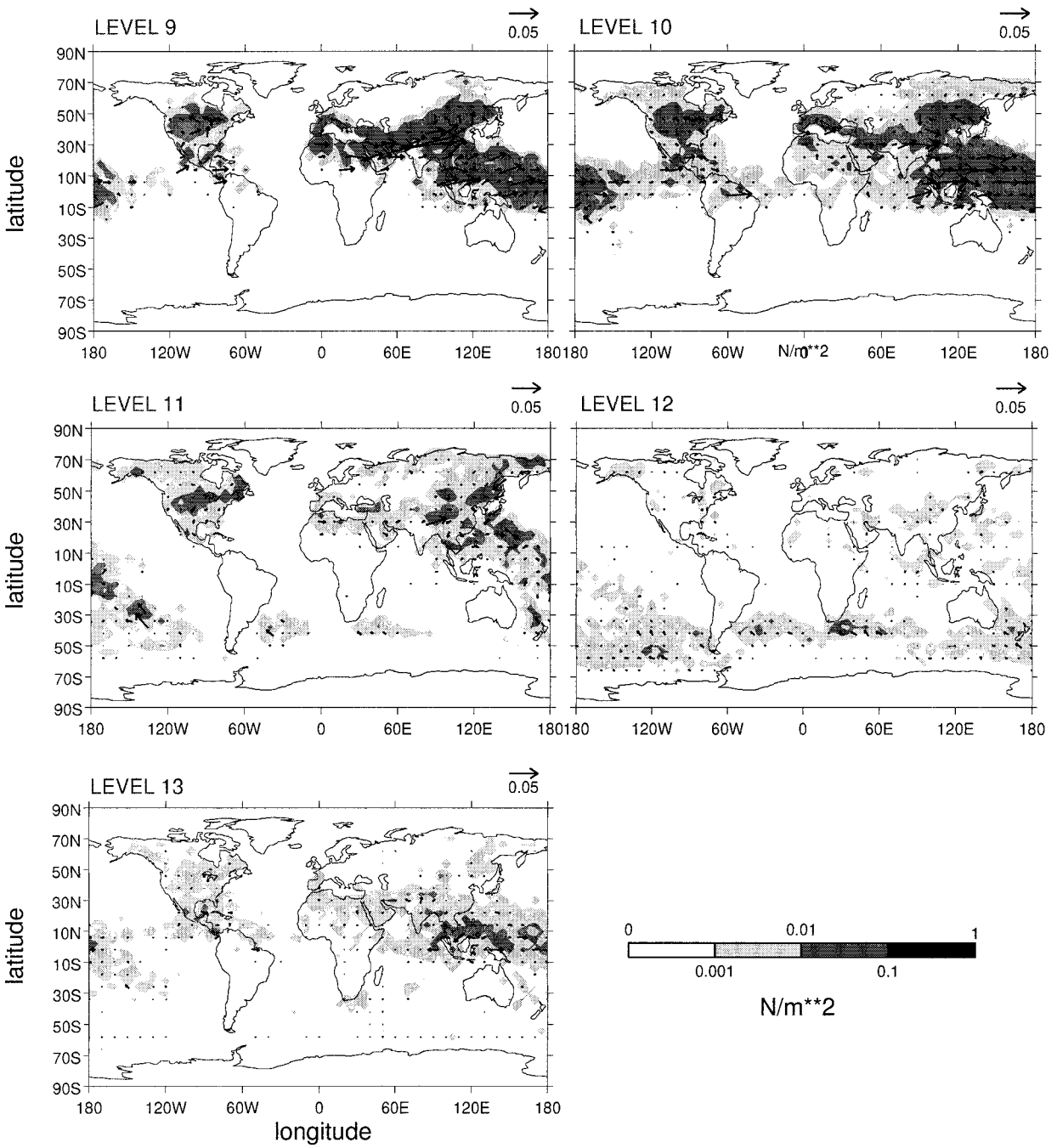

FIG. 2. The global distribution of the cloud-top gravity wave stress vector and its magnitude at levels 9–13 in the GWDC simulation. Levels 9 and 13 approximately correspond to 200 mb and PBL top, respectively. The regions greater than 0.001 N m^{-2} are shaded with different tones as indicated in the figure.

winds in the ITCZ are mostly easterly, the GWDC acts to reduce the magnitude of easterlies. The easterly acceleration below that region is due to a compensating momentum gain. The westerly deceleration in the NH midlatitude results mainly from midlevel clouds at levels 10 and 11 (Fig. 2) with a minimum value of -0.5 m s^{-1} day^{-1}.

The wave breaking appears to occur mainly in the upper troposphere and lower stratosphere before gravity waves propagate well into the stratosphere. This is different from the mountain-drag case in the YONU GCM (Chun et al. 1996), which exhibits that the wave breaking appears to occur in the upper stratosphere with a maximum zonal wind tendency of 10 m s^{-1} day^{-1} in

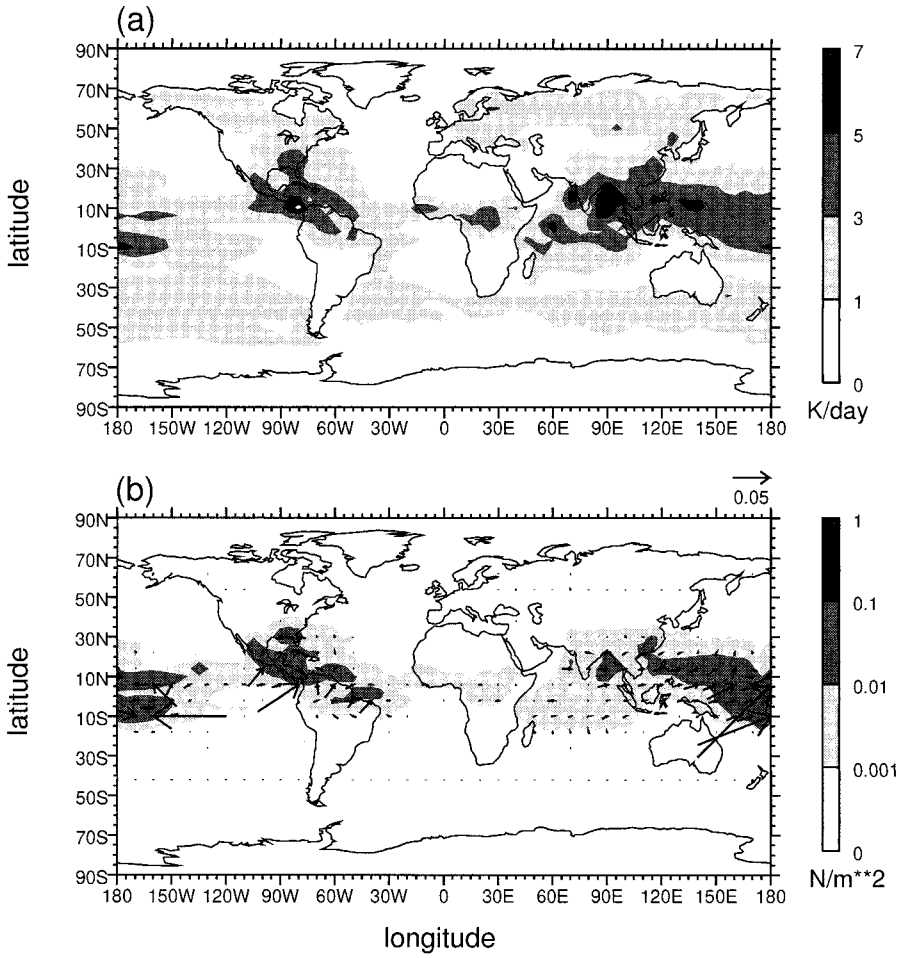

FIG. 3. The global distribution of the (a) maximum convective heating rate and (b) cloud-top gravity wave stress at 200 mb calculated using the convective heating rate in (a) and the horizontal wind and temperature from the NCEP reanalysis data in July. In (a) and (b), the regions greater than 1 K day^{-1} and 0.001 N m^{-2} are shaded, respectively, with different tones as indicated in the figures.

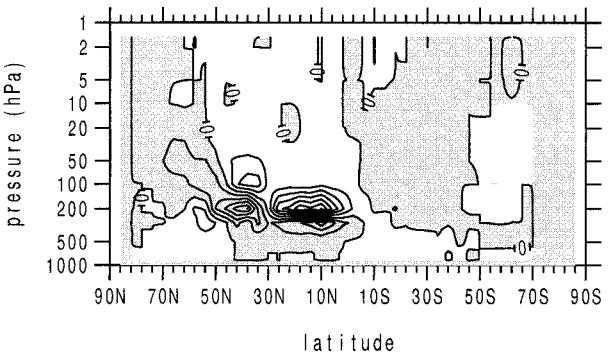

FIG. 4. The latitude–height cross section of the zonal-mean zonal wind tendency due to the GWDC parameterization. The contour interval is 0.1 m s^{-1} day^{-1}. The negative values are shaded.

January. Note that the magnitude of acceleration or deceleration due to GWD is inversely proportional to the density at wave-breaking height. Thus, the influence of GWD on the large-scale flow depends not only on the magnitude of the wave stress at a reference level (at the surface in mountain-drag case and at the cloud-top height in the GWDC case) but also on the height where the wave breaking occurs.

The effects of GWDC can be influenced by vertical resolution of the model. For given cloud-top wave stress, the sensitivity to where wave breaking occurs and how much the momentum is deposited would be reduced in coarse vertical resolution model such as the YONU GCM than high-resolution models. A further study with high vertical resolution is required.

Figure 5 shows the difference fields in the zonal-mean zonal wind and temperature between the GWDC and control simulations (GWDC simulation minus control simulation). The zonal wind difference is prominent in

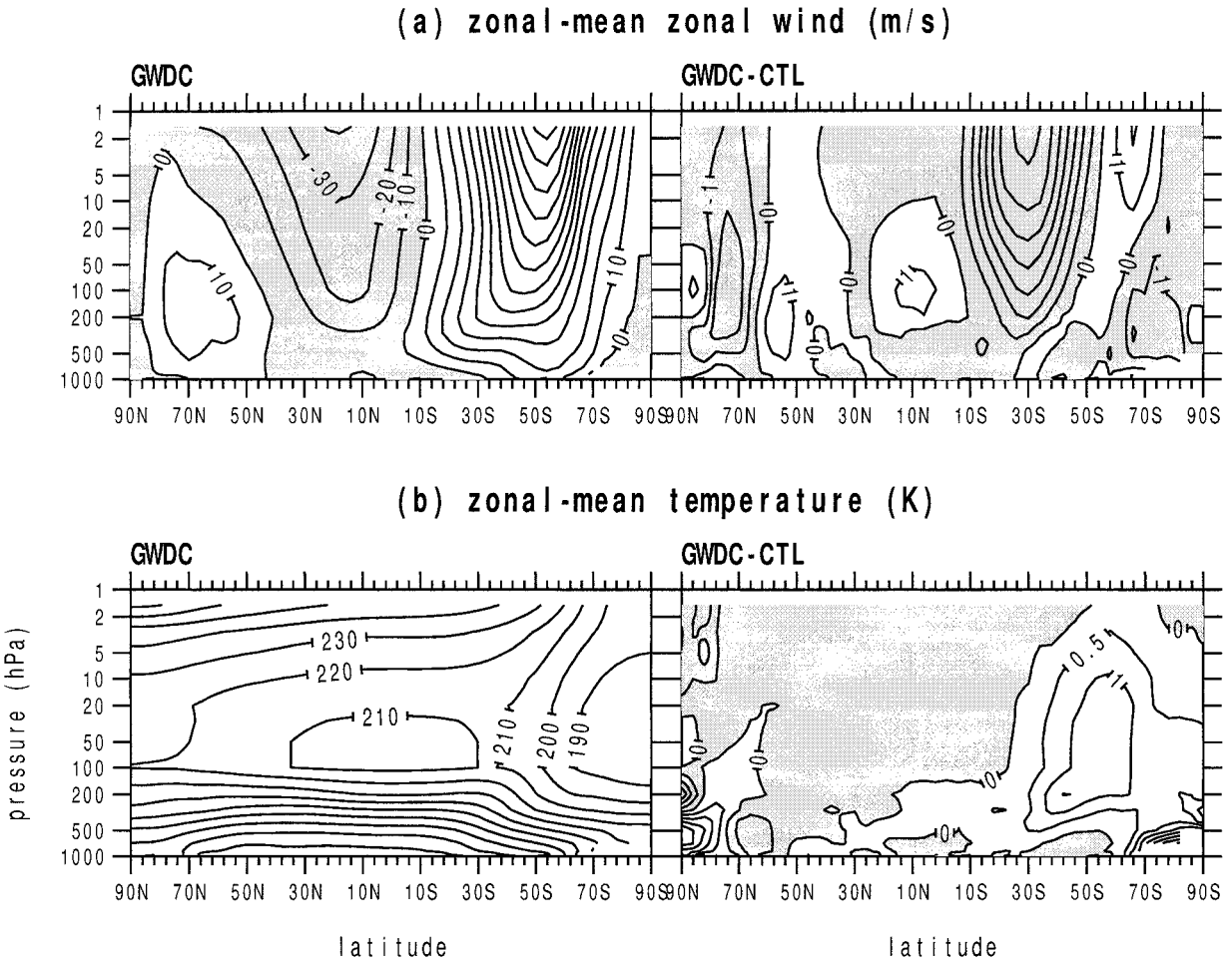

FIG. 5. The latitude–height cross section of the (a) zonal-mean zonal wind by GWDC simulation (left panel) and difference between GWDC and control simulations (right panel). (b) The same as in (a) except for the zonal-mean temperature. The contour intervals of the zonal-mean zonal wind and temperature are 10 m s^{-1} and 10 K, respectively, while those of the zonal wind and temperature differences are 1 m s^{-1} and 0.5 K, respectively. The negative values are shaded.

the SH midlatitude. The stratospheric westerly jet in the SH is reduced by as much as 7 m s^{-1} by including the GWDC parameterization. However, in the major drag forcing region of the ITCZ and in the secondary forcing region of the NH midlatitude, the zonal wind difference is less than about 1 m s^{-1}. The associated temperature difference exhibits warming in the SH middle and high latitudes by about 1 K and in the NH tropospheric polar region.

An interesting feature in Fig. 5 is that the GWDC influence is maximum in the SH midlatitude centered at 30°S, even though the maximum drag forcing is located in the ITCZ region between 10°S and 30°N (Fig. 2). Thus, some analysis of this result is needed to understand how the drag forcing by cumulus convection in the tropical region can affect the midlatitude mean flow in the SH. This understanding particularly helps to explain how the GWDC can reduce the systematic model error in the SH wintertime westerly jet reported in current GCMs.

Figure 6 shows the latitudinal variation at 200 mb of the zonal-mean zonal wind in the control and GWDC simulations and the zonal wind difference between the two simulations. The GWDC forcing at the same level is superimposed in Fig. 6. The drag forcing by convectively generated internal gravity waves is the largest at 200 mb. It is positive in the ITCZ with easterly mean flow and deep cumulus clouds, but is negative in the NH midlatitude with westerly mean flow and midlevel cumulus clouds. In the SH outside the ITCZ, there is almost no drag forcing. However, the magnitude of the zonal wind difference between the GWDC and control simulations in the SH middle and high latitudes are comparable to that in the forcing region. Figure 6 suggests that planetary waves are activated by the GWDC in the SH where strong westerlies exist. This is clearly

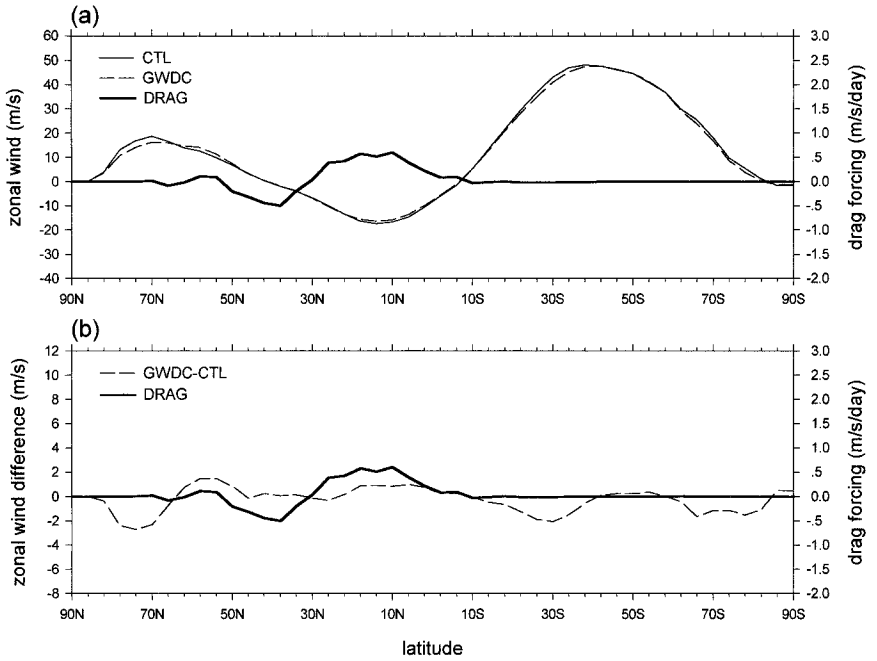

FIG. 6. The latitudinal variation of the (a) zonal-mean zonal wind in the control and GWDC simulations at 200 mb and (b) zonal-mean zonal wind difference between the GWDC and control simulations at 200 mb. The GWDC forcing at 200 mb is superimposed in (a) and (b).

indicated in Fig. 7, which is the same as Fig. 6 except for at 10 mb. There is almost no drag forcing at 10 mb because the wave breaking appears to occur in the upper troposphere and lower stratosphere. However, the influence of GWDC on the zonal wind is much larger than that at 200 mb where the main drag forcing is present. The dominancy of the GWDC effect in the SH westerly region suggests that vertically propagating planetary waves that are allowed in the westerly flow are responsible for changing the zonal-mean flow.

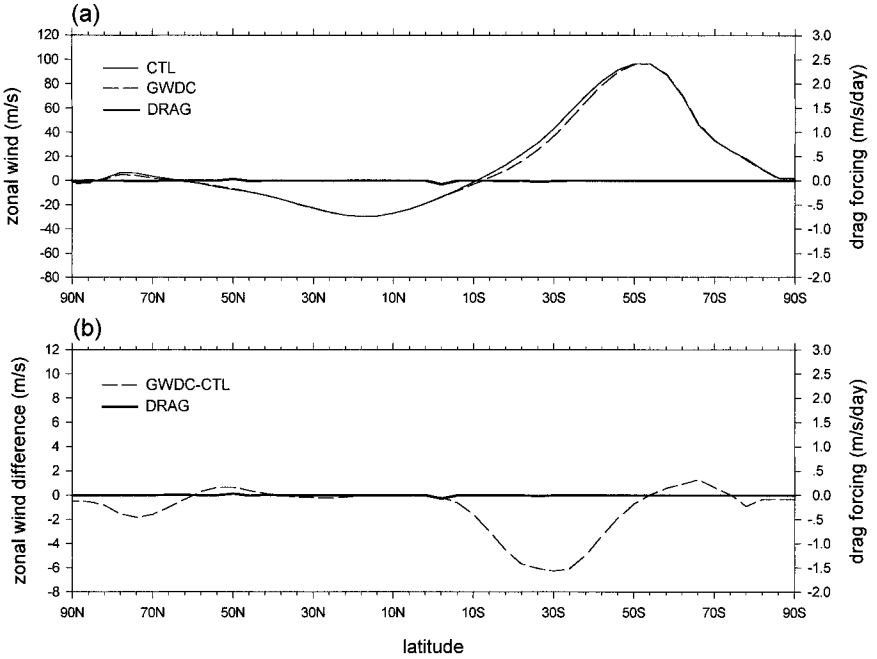

FIG. 7. The same as in Fig. 6 except for at 10 mb.

In the mountain-induced GWD case (e.g., Chun et al. 1996), the main impact of GWD on the zonal flow in the NH wintertime occurs in the region of drag forcing. It is worth understanding a situational difference between the mountain-induced GWD case in the NH wintertime and the present GWDC case in the SH wintertime. In the mountain-drag case, the major forcing region is located in the NH midlatitude where westerly jets exist. On the other hand, in the present GWDC case, the drag forcing is located in the ITCZ with the easterly mean flow. This difference results from the asymmetry of the drag forcing with respect to each hemisphere, even though the stratospheric zonal flow is seasonally reversed with respect to each hemisphere.

In the mountain-drag case, the GWD influence can be well examined using linear theory of the zonal-mean flow in terms of the secondary circulation induced by drag forcing (Palmer et al. 1986). The secondary circulation induced by localized drag forcing can be latitudinally confined near the forcing region. That is, the latitudinal teleconnection between the forcing and response regions through waves may not be necessarily considered. Surprisingly, little studies have been done to seriously examine the influence of GWD by mountains on planetary waves. Holton (1984) showed that the longitudinally asymmetric gravity wave drag excites a planetary wave of zonal wavenumber 1 in the mesosphere, which has the maximum value at one-quarter cycle upstream of the drag-forcing region. Pierrehumbert (1986) investigated the generation of Rossby waves by specified GWD forcing using a linearized, steady-state, barotropic vorticity equation on a midlatitude β plane. He showed that the localized drag forcing can excite a free Rossby wave in the lee side of the forcing region in both the north and south of the forcing center. Using a simplified GCM, he showed that the simulated wave pattern in the northern part of the drag forcing is similar to linear Rossby waves and that in the southern part does not appear in the model result because the zonal wind becomes easterly when approaching equatorward from 30°N. Therefore, the influence of mountain drag is confined within the NH middle and high latitudes, even though planetary waves are considered.

In the present GWDC case, the drag source is located in the ITCZ with the easterly mean flow. Planetary waves generated by the drag forcing can propagate vertically and latitudinally (both northward and southward) into the region where the mean flow is westerly. This makes a theoretical approach difficult compared to the mountain-drag case by Pierrehumbert (1986). This is because the propagation can be confined within neither midlatitude nor tropical area, but in global area.

3) Effects of GWDC on planetary waves

In order to examine the effects of GWDC on planetary waves, wave analyses at 200 and 10 mb are performed. Figure 8 shows the geopotential height perturbation fields at 200 mb in the control and GWDC simulations and their difference between the two simulations. Since the geopotential height field is averaged for the last 90 days, the waves in Fig. 8 are stationary planetary waves. It is shown that such stationary planetary waves are dominant in the major westerly regions in the middle and high latitudes of both the hemispheres. The amplitude of the geopotential height perturbation is larger in the SH than in the NH. The zonal wavenumber 1 structure is clearly seen in the SH, while a combination of zonal wavenumbers 1 and 2 appears in the NH. Figure 8 indicates that the GWDC process enhances the wave amplitude in the high latitudes of both the hemispheres.

At 10 mb (Fig. 9), the NH wave amplitude in the control simulation is smaller than that at 200 mb, while the SH wave amplitude is larger than that at 200 mb. This is because vertically propagating planetary waves cannot reach near 10 mb in the NH where easterly mean flow exists. The zonal wavenumber 1 structure is clearly seen in the SH where westerlies exist, which is extended equatorward (as far as 10°S). Figure 9 shows that the GWDC process enhances the wave amplitude significantly in the middle and high latitudes of the SH.

The effects of GWDC on the vertical structure of individual wave modes are examined by performing the spectral analysis of the geopotential height perturbation. Figure 10 shows the difference between the GWDC and control simulations in the wave amplitude of the geopotential height perturbation for zonal wavenumbers 1 and 2. The wave amplitude of zonal wavenumber 1 increases in the high latitudes of both the hemispheres centered near 70° lat in the upper troposphere. A secondary maximum is observed in the SH upper stratosphere at about 35°S. Compared to the NCEP reanalysis data (now shown), the increased amplitude of wavenumber 1 in the SH high latitude significantly reduces the model error in the geopotential height field, while that in the NH high latitude increases the existing bias of the excessive wave amplitude in the control simulation. The wave amplitude of zonal wavenumber 1 extends too high in the NH high latitudes in both the control and GWDC simulations. This is because the westerly flow in the NH reaches too high compared to the observations. On the other hand, the wave amplitude of zonal wavenumber 2 significantly increases (more than three times compared to the control simulation) in the SH upper stratosphere and slightly decreases in the NH by the GWDC process. Compared to the NCEP reanalysis data (not shown), this change in the wave amplitude of wavenumber 2 reduces the model error in both hemispheres. Especially, the amplitude of wavenumber 2 in the SH midlatitude significantly increases by the GWDC process, thus being closer to the observations.

The simulated amplitudes of planetary waves of zonal wavenumbers 1 and 2 are compared in Fig. 11 with observation both in the upper troposphere with the major drag forcing and in the upper stratosphere. The upper panels show the amplitudes of the geopotential height perturbation for zonal wavenumber 1 in the control sim-

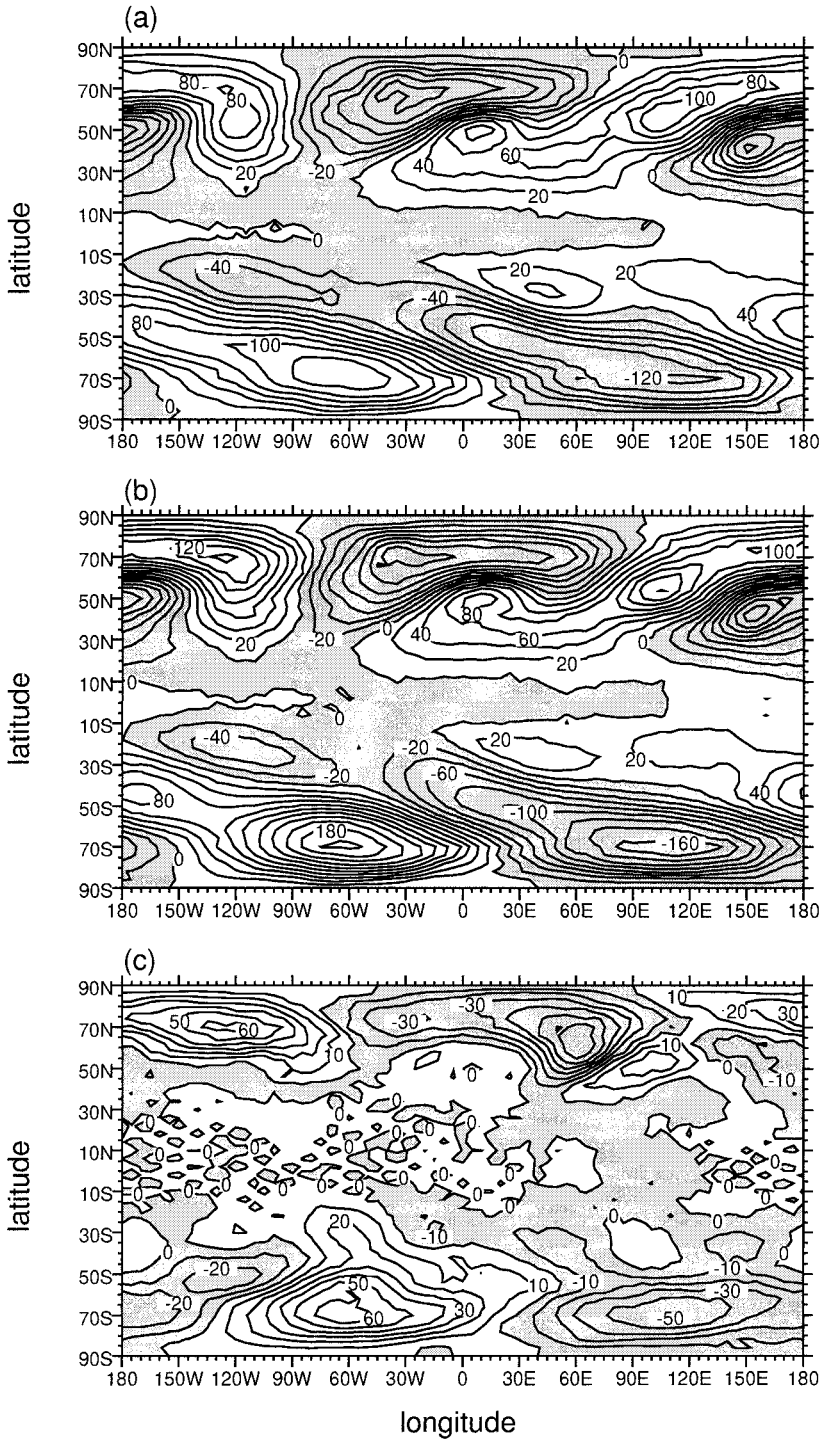

FIG. 8. The global distribution of the geopotential height perturbation at 200 mb in the (a) control simulation, (b) GWDC simulation, and (c) its difference between the two simulations. The contour intervals in (a), (b), and (c) are 20, 20, and 10 m, respectively. The negative values are shaded.

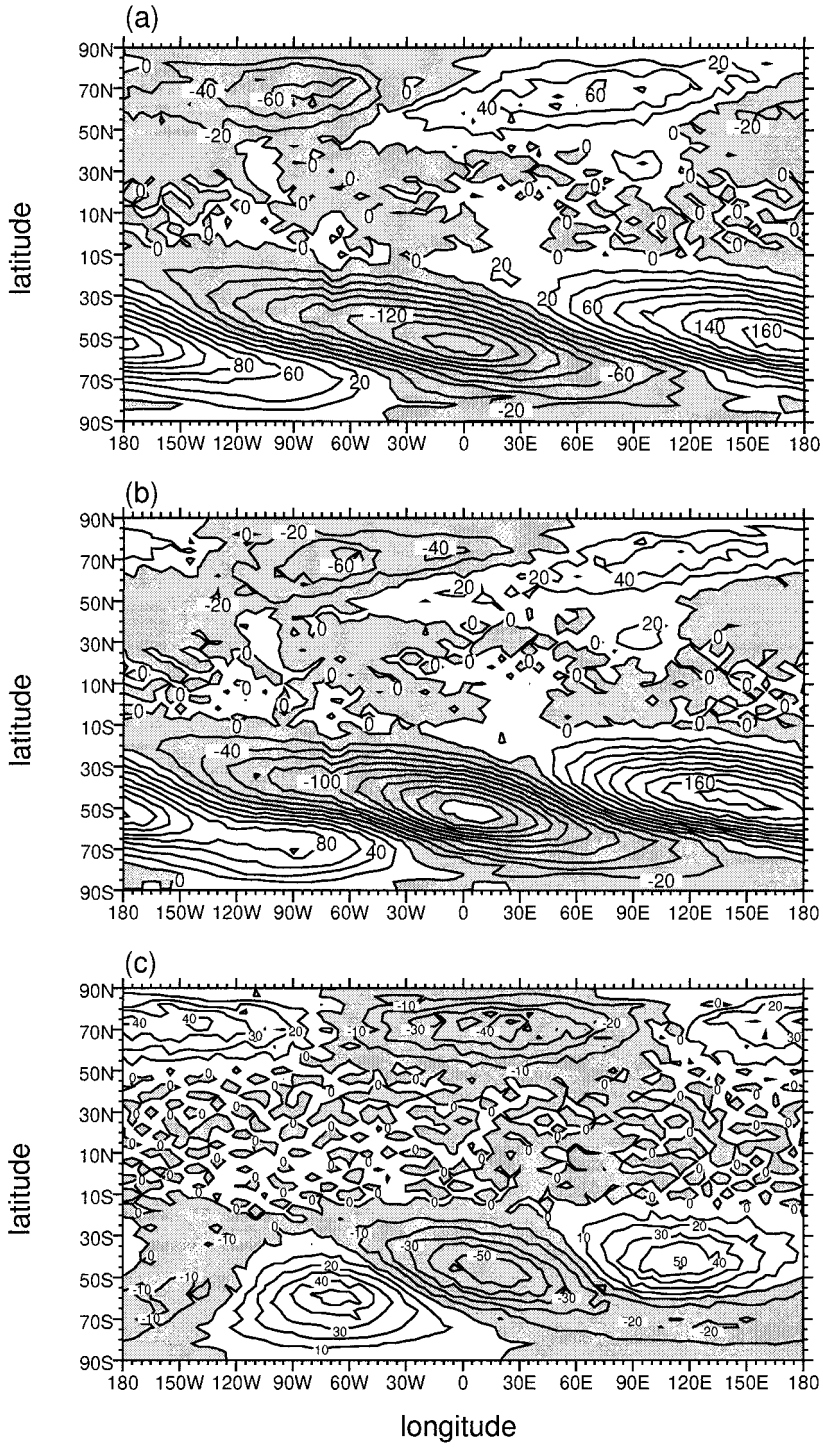

FIG. 9. The same as in Fig. 8 except for at 10 mb.

ulation, GWDC simulation, and NCEP reanalysis data at 10 and 200 mb, respectively. The lower panels show the same as in the upper panels except for zonal wavenumber 2. Figure 11a shows that the GWDC process increases the wave amplitude of wavenumber 1 slightly in the SH midlatitude, but decreases it in the NH high latitude. However, the simulated amplitude is much smaller than observed in the SH high latitude and slightly larger than that in the NH high latitude. The GWDC process, however, significantly increases the amplitude

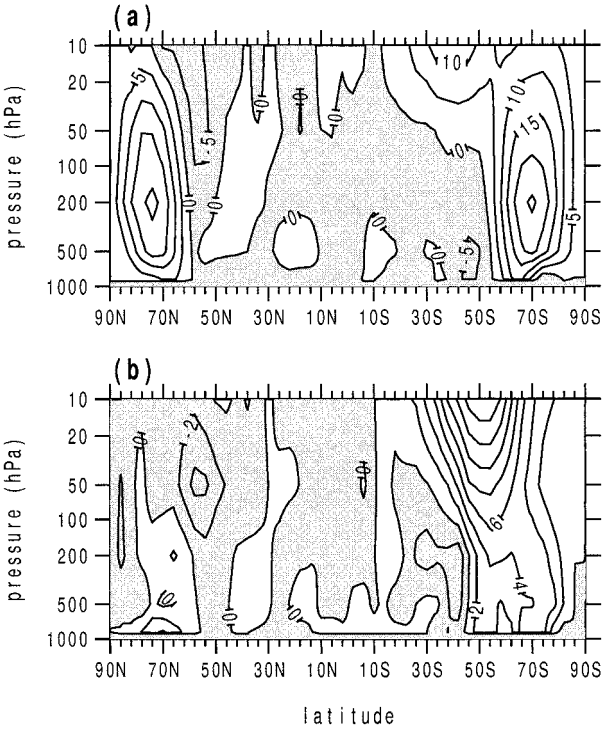

FIG. 10. The latitude–height cross section of the difference in the zonal-mean vertical structure of the wave amplitude of the geopotential height perturbation between the GWDC and control simulations: (a) zonal wavenumber 1 and (b) zonal wavenumber 2. The contour intervals in (a) and (b) are 5 m and 2 m, respectively.

of wavenumber 2 in the SH middle and high latitudes at 10 mb, thus being closer to the observed value. At 200 mb (Fig. 11b), the GWDC process increases the amplitude of wavenumber 1 in the high latitudes of both the hemispheres, while it increases the amplitude of wavenumber 2 in the SH high latitude ($>50°$S), but decreases the amplitude in the SH midlatitude. A significant discrepancy is found in the amplitude of wavenumber 2 at 200 mb between the simulations and the observations in the NH midlatitude.

It seems that the amplification of planetary waves of wavenumbers 1 and 2 by the GWDC process in the SH middle and high latitudes is responsible for reducing the zonal wind in the upper stratosphere (Figs. 5a and 7b), even though the drag forcing is localized in the ITCZ. This result is consistent to some extent with that by Rind et al. (1988b), who showed that the zonal-mean flow changes by complex interactions between the mean flow, GWD, and planetary waves, with multiple feedbacks. Based on the GCM simulation results with GWD parameterization by mountains, moist convection, and shear instability, they suggested that GWD would help cause planetary waves to decelerate zonal-mean flow by providing a cause for violation of the conditions for the nonacceleration theorem. In the present study, we emphasize the GWDC effects in the SH wintertime, while they focused on the NH wintertime and sudden warming events.

Figure 12 shows the difference between the GWDC and control simulations in the zonal-mean stationary eddy kinetic energy and Eliassen–Palm (EP) flux di-

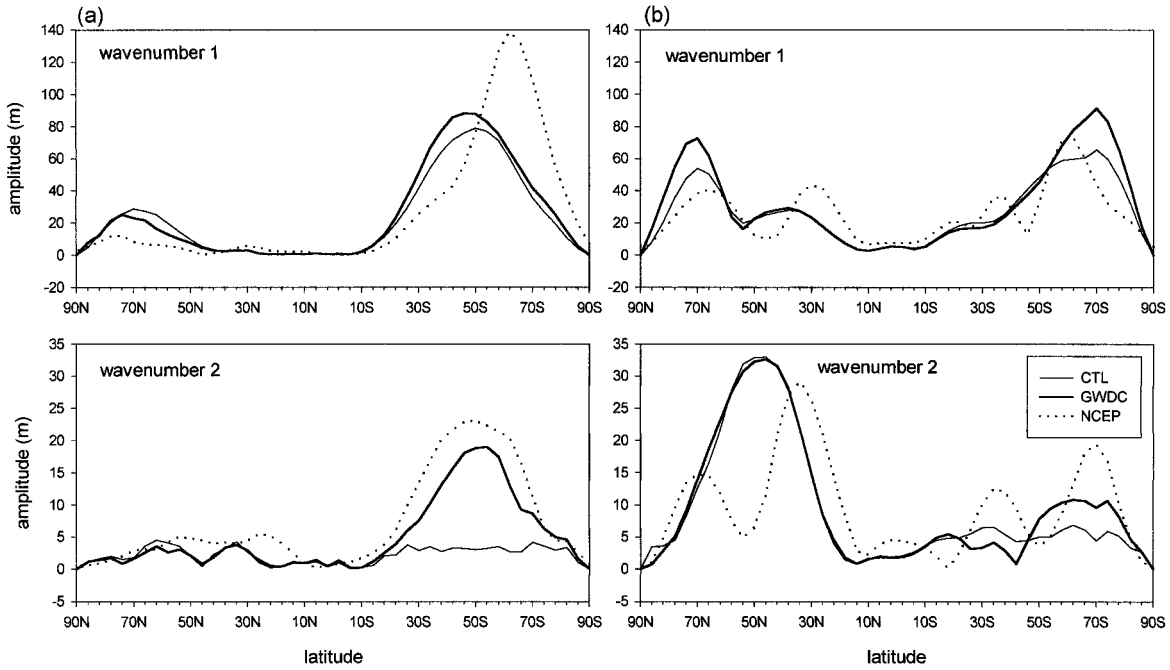

FIG. 11. (a) The latitudinal variation of the wave amplitude of the geopotential height perturbation for zonal wavenumber 1 (upper panel) and zonal wavenumber 2 (lower panel) at 10 mb in the control simulation (thin line), GWDC simulation (thick line), and NCEP reanalysis data (dotted line). (b) The same as in (a) except for at 200 mb.

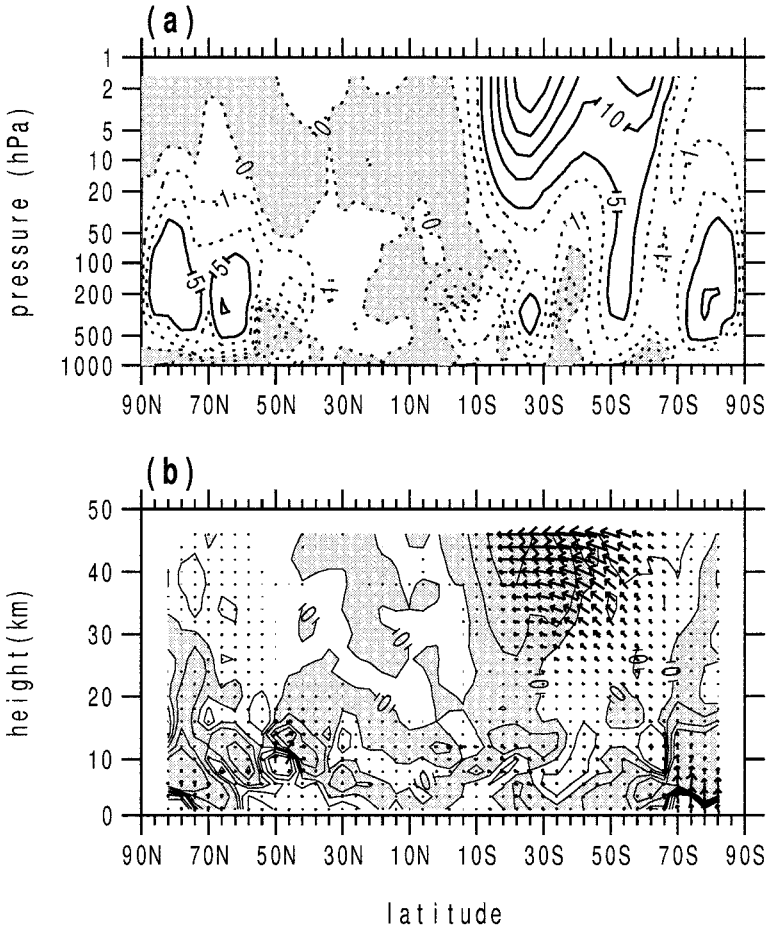

FIG. 12. The latitude–height cross section of the difference between the GWDC and control simulations in the (a) zonal-mean stationary eddy kinetic energy ($m^2\ s^{-2}$) and (b) zonal-mean Eliassen–Palm (EP) flux divergence forcing ($m\ s^{-1}\ day^{-1}$) superimposed on the EP flux vector ($kg\ m^{-1}\ s^{-2}$).

vergence forcing ($m\ s^{-1}\ day^{-1}$) superimposed on the EP flux vector. Note that the EP flux divergence forcing is obtained by dividing the EP flux divergence by $\rho_0 a \cos\phi$, where ρ_0 is the basic-state density, a the radius of the Earth, and ϕ the latitude, in order to calculate the wind tendency directly. It is shown that the GWDC process significantly enhances the eddy kinetic energy in the SH upper stratosphere in the low and middle latitudes centered near 30°S where the zonal wind is mostly reduced by the GWDC process, as shown in Fig. 5a. On the other hand, in the NH, the eddy kinetic energy is slightly increased by the GWDC process in the high-latitude upper troposphere and lower stratosphere where westerlies are extended. This feature is related to the amplification of stationary planetary waves by the GWDC process (Fig. 9). The difference in the EP flux vector between the GWDC and control simulations indicates that the GWDC process enhances the vertical component of the EP flux vector in the troposphere of the SH high latitude and the horizontal component of the EP flux vector in the upper stratosphere of the SH midlatitude. This implies that in the high latitude the heat transport by stationary waves is dominant, while in the midlatitude the momentum transport by stationary waves is dominant.

The EP flux divergence forcing (Fig. 12b) is negative (westerly deceleration) in the SH stratosphere in the low and middle latitudes, and also in the mid- and high-latitude tropospheres of both the hemispheres. In the SH midlatitude stratosphere, the EP flux vector turning equatorward is enhanced by the GWDC process in association with the enhanced wave activity there. In the NH, there is no major effect of GWDC on the EP flux vector in the stratosphere. This is also related to the amplification of stationary planetary waves of zonal wavenumbers 1 and 2, as shown in Fig. 9.

5. Summary and conclusions

A parameterization scheme for gravity wave drag induced by cumulus convection (GWDC) proposed by

Chun and Baik (1998) was implemented in the YONU GCM to investigate the effects of GWDC on the mean flow and planetary waves through perpetual July simulations. The GWDC parameterization scheme used in the present study was a modified version of CB, which includes a momentum gain in the cloud region to conserve the momentum.

It was shown that the gravity wave stress at the cloud top is concentrated in the ITCZ (10°S–30°N) with its maximum value of 0.14 N m^{-2}. Since the magnitude of the wave stress is inversely proportional to the wind speed and atmospheric stability, the wave stress in high latitudes is relatively small due to the large wind speed and stability. Wave breaking appears to occur mainly in the upper troposphere and lower stratosphere. This is different from the mountain-induced GWD parameterization case in which the wave breaking appears to occur in the upper stratosphere (e.g., Palmer et al. 1986; Chun et al. 1996). As a result, the magnitude of acceleration/deceleration becomes smaller than that in the mountain-induced GWD parameterization case. The major positive (westerly acceleration) gravity wave drag forcing exists in the easterly region of the ITCZ by deep cumulus clouds and the negative (easterly acceleration) drag forcing exists in the westerly region of the NH midlatitude mainly by midlevel cumulus clouds. The maximum value of the westerly acceleration by the GWDC process is 0.6 m s^{-1} day^{-1}. This value is close to that observed by Pfister et al. (1993).

The zonal-mean zonal wind difference between the GWDC and control simulations revealed an unexpected feature that the zonal wind difference is predominant in the stratosphere of the SH midlatitude where major westerly jet exists rather than in the major forcing region. The excessive westerly jet in the region that appeared in the control simulation is reduced by as much as 7 m s^{-1} by including the GWDC parameterization. This implies that a nonlinear process through planetary wave activity might play an important role in changing the zonal-mean flow rather than by direct drag forcing. This hypothesis is evidenced by analyzing planetary waves with the geopotential height field. It was shown that the GWDC process enhances stationary waves of zonal wavenumbers 1 and 2 in the SH middle and high latitudes and NH high latitude. Especially, the amplitude of wavenumber 2 increases significantly in the SH midlatitude where a westerly jet exists. The model bias in stationary waves is significantly alleviated. The eddy kinetic energy and Eliassen–Palm flux divergence fields clearly indicated that stationary planetary waves induced and/or excited by the GWDC process are responsible for changing the zonal-mean flow in the stratosphere of the SH midlatitude. This result is encouraging in that including GWDC parameterization can alleviate the excessive westerly bias in the SH wintertime and associated cold temperature bias in the SH polar region, which have been reported in many GCMs.

In order to understand how planetary waves induced by the drag forcing in the ITCZ can be excited in the SH midlatitude, wave propagation mechanisms should be taken into account. However, the propagation of planetary waves could not be explicitly considered in this study because of the perpetual July simulation, even though the latitude–height cross section of analyzed planetary waves reveals the selective vertical propagation of planetary waves in the westerly flow region consistently with the Charney-Drazin theorem (Charney and Drazin 1961). Compared to the mountain-induced GWD parameterization case, a mathematical difficulty for dealing with the wave propagation exists in the present case. Since the major drag forcing is located in the ITCZ with easterlies bounded by critical latitudes with zero zonal-mean flow, planetary waves generated by the drag forcing can propagate into the westerly region in both the hemispheres. This situation is different from the mountain drag case in the NH wintertime in which the major forcing is located in the NH midlatitude with westerlies and the wave propagation is confined within the NH midlatitude by the reflection of waves at the critical latitude near 30°N. Therefore, in the present study, wave propagation should be considered globally rather than just in a midlatitude or tropical β plane.

In this study, the effects of GWDC in the tropical region are not fully investigated. Even though the magnitude of the zonal wind difference between GWDC and control simulations (Fig. 5a) is maximum in the SH midlatitude of westerly jet because the zonal wind itself is maximum in that region, the ratio of the zonal wind difference to the zonal wind (not shown) in the tropical region is comparable to that in the SH midlatitude. Because the GWDC process can either decelerate the mean flow by direct drag forcing or accelerate the mean flow indirectly through the secondary circulation, planetary waves, and nonlinear advection processes, GWDC may play an important role in QBO dynamics. However, the present study using a coarse vertical resolution model has a limitation for applying the results to QBO phenomena. The sensitivity to where wave breaking occurs and how much the momentum flux is deposited would be reduced in the present coarse vertical resolution model (15 layers) than high vertical resolution models, which can simulate QBO-like signals [e.g., 80 layers SKIHI model used in Hamilton et al. (1999)]. Investigation of GWDC impact on QBO dynamics using a high vertical resolution model remains to be done.

Acknowledgments. The authors are very grateful to two anonymous reviewers for their constructive suggestions, which improved this paper. The authors also would like to thank Prof. Carlos Mechoso at UCLA for providing valuable comments on this research and Prof. Hyeong-Bin Cheong at Pukyong National University for providing valuable references on stratospheric planetary waves. Thanks are also due to Drs. Jun-Hee Jung and Il-Ung Chung for their help in our using the YONU GCM. A part of this research was performed while the

last author (JJB) was visiting Yonsei University on his sabbatical leave. This work is supported by 1999-1-134-001-5 from the Basic Research Program of the Korea Science and Engineering Foundation and the Ministry of Environment of Korea through the G7 project on technology for climate change prediction. This work was also supported by the Brain Korea 21 Program.

REFERENCES

Alexander, M. J., and J. R. Holton, 1997: A model study of zonal forcing in the equatorial stratosphere by convectively induced gravity waves. *J. Atmos. Sci.,* **54,** 408–419.

——, ——, and D. R. Durran, 1995: The gravity wave response above deep convection in a squall line simulation. *J. Atmos. Sci.,* **52,** 2212–2226.

Alexander, R. C., and R. L. Mobley, 1976: Monthly averaged sea surface temperatures and ice pack limits on a 1° global grid. *Mon. Wea. Rev.,* **104,** 143–148.

Allen, S., and R. A. Vincent, 1995: Gravity wave activity in the lower atmosphere: Seasonal and latitudinal variations. *J. Geophys. Res.,* **100,** 1327–1350.

Arakawa, A., and W. H. Schubert, 1974: Interaction of a cumulus cloud ensemble with the large-scale environment, Part I. *J. Atmos. Sci.,* **31,** 674–701.

Charney, J. G., and P. G. Drazin, 1961: Propagation of planetary-scale disturbances from the lower into the upper atmosphere. *J. Geophys. Res.,* **66,** 83–110.

Chun, H.-Y., and J.-J. Baik, 1998: Momentum flux by thermally induced internal gravity waves and its approximation for large-scale models. *J. Atmos. Sci.,* **55,** 3299–3310.

——, J.-H. Jung, J.-H. Oh, and J.-W. Kim, 1996: Effects of mountain-induced gravity wave drag on atmospheric general circulation. *J. Korean Meteor. Soc.,* **32,** 581–592.

Fovell, R., D. Durran, and J. R. Holton, 1992: Numerical simulations of convectively generated stratospheric gravity waves. *J. Atmos. Sci.,* **49,** 1427–1442.

Fritts, D. C., 1984: Gravity wave saturation in the middle atmosphere: A review of theory and observations. *Rev. Geophys. Space Phys.,* **22,** 275–308.

Gregory, D., R. Kershaw, and P. M. Inness, 1997: Parameterization of momentum transport by convection. II: Tests in single-column and general circulation models. *Quart. J. Roy. Meteor. Soc.,* **123,** 1153–1183.

Guinn, T. A., 1989: A modeling study of the cloud-topped marine boundary layer. Atmospheric Science Paper 458, Colorado State University, 63 pp. [Available from Department of Atmospheric Science, Colorado State University, Fort Collins, CO 80523.]

Hamilton, K., 1983: Diagnostic study of the momentum balance in the Northern Hemisphere winter stratosphere. *Mon. Wea. Rev.,* **111,** 1434–1441.

——, 1997: The role of parameterized drag in a troposphere-stratosphere-mesosphere general circulation model. *Gravity Wave Processes: Their Parameterization in Global Climate Models,* K. Hamilton, Ed., Springer-Verlag, 337–350.

——, R. J. Wilson, and R. S. Hemler, 1999: Middle atmosphere simulated with high vertical and horizontal resolution versions of a GCM: Improvements in the cold bias and generation of a QBO-like oscillation in the Tropics. *J. Atmos. Sci.,* **56,** 3829–3846.

Hines, C. O., 1991: The saturation of gravity waves in the middle atmosphere. Part II: Development of Doppler-spread theory. *J. Atmos. Sci.,* **48,** 1360–1379.

Hoinka, K. P., 1985: Observation of the airflow over the Alps during a foehn event. *Quart. J. Roy. Meteor. Soc.,* **111,** 199–224.

Holloway, J. L., Jr., and S. Manabe, 1971: Simulation of climate by a general circulation model. Part I: Hydrological cycle and heat balance. *Mon. Wea. Rev.,* **99,** 335–370.

Holton, J. R., 1983: The influence of gravity wave breaking on the general circulation of the middle atmosphere. *J. Atmos. Sci.,* **40,** 2497–2507.

——, 1984: The generation of mesospheric planetary waves by zonally asymmetric gravity wave breaking. *J. Atmos. Sci.,* **41,** 3427–3430.

Kershaw, R., 1995: Parameterization of momentum transport by convectively generated gravity waves. *Quart. J. Roy. Meteor. Soc.,* **121,** 1023–1040.

Lilly, D. K., 1968: Models of cloud-topped mixed layers under a strong inversion. *Quart. J. Roy. Meteor. Soc.,* **94,** 292–309.

Lindzen, R. S., 1981: Turbulence and stress due to gravity wave and tidal breakdown. *J. Geophys. Res.,* **86,** 9707–9714.

——, 1984: Gravity waves in the middle atmosphere. *Dynamics of the Middle Atmosphere,* J. R. Holton and T. Matsuno, Eds., Terra, 3–18.

Louis, J.-F., 1979: A parametric model of vertical eddy fluxes in the atmosphere. *Bound.-Layer Meteor.,* **17,** 187–202.

Manabe, S., 1969: Climate and the ocean circulation. Part I. The atmospheric circulation and the hydrology of the earth's surface. *Mon. Wea. Rev.,* **97,** 739–774.

Manzini, E., and L. Bengtsson, 1996: Stratospheric climate and variability from a general circulation model and observations. *Climate Dyn.,* **12,** 615–639.

McFarlane, N. A., 1987: The effects of orographically excited gravity wave drag on the general circulation of the lower stratosphere and troposphere. *J. Atmos. Sci.,* **44,** 1775–1800.

Medvedev, A. S., and G. P. Klaassen, 1995: Vertical evolution of gravity wave spectra and the parameterization of associated wave drag. *J. Geophys. Res.,* **100,** 25 841–25 853.

——, ——, and S. R. Beagley, 1998: On the role of an anisotropic gravity wave spectrum in maintaining the circulation of the middle atmosphere. *Geophys. Res. Lett.,* **25,** 509–512.

Norton, W. A., and J. Thuburn, 1997: The mesosphere in the extended UGAMP GCM. *Gravity Wave Processes: Their Parameterization in Global Climate Models,* K. Hamilton, Ed., Springer-Verlag, 384–401.

Oh, J.-H., 1989: Physically-based general circulation model parameterization of clouds and their radiative interaction. Ph.D. dissertation, Oregon State University, 315 pp. [Available from University Microfilm, 305 N. Zeeb Rd., Ann Arbor, MI 48106.]

Palmer, T. N., G. J. Shutts, and R. Swinbank, 1986: Alleviation of a systematic westerly bias in circulation and numerical weather prediction model through an orographic gravity wave drag parameterization. *Quart. J. Roy. Meteor. Soc.,* **112,** 1001–1039.

Pfister, L., S. Scott, and M. Loewenstein, 1993: Mesoscale disturbance in the tropical stratosphere excited by convection: Observations and effects on the stratospheric momentum budget. *J. Atmos. Sci.,* **50,** 1058–1075.

Pierrehumbert, R. T., 1986: An essay on the parameterization of orographic gravity wave drag. *Proc. Seminar/Workshop on Observation, Theory and Modeling of Orographic Effects,* Vol. 1, Reading, United Kingdom, ECMWF, 251–282.

Randall, D. L., 1976: The interaction of the planetary boundary layer with large-scale circulations. Ph.D. dissertation, University of California, Los Angeles, 247 pp. [Available from University Microfilm, 305 N. Zeeb Rd., Ann Arbor, MI 48106.]

Rind, D., R. Suozzo, N. K. Balachandran, A. Lacis, and G. Russel, 1988a: The GISS global climate–middle atmosphere model. Part I: Model structure and climatology. *J. Atmos. Sci.,* **45,** 329–370.

——, ——, and ——, 1988b: The GISS global climate-middle atmosphere model. Part II: Model variability due to interactions between planetary waves, the mean circulation and gravity wave drag. *J. Atmos. Sci.,* **45,** 371–386.

Schlesinger, M. E., J.-H. Oh, and D. Rosenfeld, 1988: A parameterization of the evaporation of rainfall. *Mon. Wea. Rev.,* **116,** 1887–1895.

Smith, A. K., and L. V. Lyjak, 1985: An observational estimate of gravity wave drag from the momentum balance in the middle atmosphere. *J. Geophys. Res.,* **90,** 2233–2241.

Stratton, R. A., 1999: A high resolution AMIP integration using the Hadley Centre model HadAM2b. *Climate Dyn.,* **15,** 9–28.

Sundqvist, H., 1988: Parameterization of condensation and associated clouds in models for weather prediction and general circulation simulation. *Physically-based Modelling and Simulation of Climate and Climatic Change,* M. E. Schlesinger, Ed., Reidel, 433–462.

Tokioka, T., 1978: Some consideration on vertical differencing. *J. Meteor. Soc. Japan,* **56,** 98–111.

Wu, X., and M. Moncrieff, 1996: Collective effects of organized convection and their approximation in general circulation models. *J. Atmos. Sci.,* **53,** 1477–1495.